

Pressure-induced Superconductivity and Structure Phase Transition in SnAs-based Zintl Compound SrSn_2As_2

Weizheng Cao^{1#}, Juefei Wu^{1#}, Yongkai Li^{2,3,4#}, Cuiying Pei¹, Qi Wang^{1,5}, Yi Zhao¹, Changhua Li¹, Shihao Zhu¹, Mingxin Zhang¹, Lili Zhang⁶, Yulin Chen^{1,5,7}, Zhiwei Wang^{2,3,4*}, Yugui Yao^{2,3}, and Yanpeng Qi^{1,2,8*}

1. School of Physical Science and Technology, ShanghaiTech University, Shanghai 201210, China
2. Centre for Quantum Physics, Key Laboratory of Advanced Optoelectronic Quantum Architecture and Measurement (MOE), School of Physics, Beijing Institute of Technology, Beijing 100081, China
3. Beijing Key Lab of Nanophotonics and Ultrafine Optoelectronic Systems, Beijing Institute of Technology, Beijing 100081, China
4. Material Science Center, Yangtze Delta Region Academy of Beijing Institute of Technology, Jiaxing, 314011, China
5. ShanghaiTech Laboratory for Topological Physics, ShanghaiTech University, Shanghai 201210, China
6. Shanghai Synchrotron Radiation Facility, Shanghai Advanced Research Institute, Chinese Academy of Sciences, Shanghai 201203, China
7. Department of Physics, Clarendon Laboratory, University of Oxford, Parks Road, Oxford OX1 3PU, UK
8. Shanghai Key Laboratory of High-resolution Electron Microscopy, ShanghaiTech University, Shanghai 201210, China

These authors contributed to this work equally.

* Correspondence should be addressed to Y.Q. (qiyp@shanghaitech.edu.cn) or Z.W. (zhiweiwang@bit.edu.cn)

ABSTRACT

Layered SnAs-based Zintl compounds exhibit a distinctive electronic structure, igniting extensive research efforts in areas of superconductivity, topological insulators and quantum magnetism. In this paper, we systematically investigate the crystal structures and electronic properties of the Zintl compound SrSn_2As_2 under high-pressure. At approximately 20.8 GPa, pressure-induced superconductivity is observed in SrSn_2As_2 with a characteristic dome-like evolution of T_c . Theoretical calculations together with high pressure synchrotron X-ray diffraction and Raman spectroscopy have identified that SrSn_2As_2 undergoes a structural transformation from a trigonal to a monoclinic structure. Beyond 28.3 GPa, the superconducting transition temperature is suppressed due to a reduction of the density of state at the Fermi level. The discovery of pressure-induced superconductivity, accompanied by structural transitions in SrSn_2As_2 , greatly expands the physical properties of layered SnAs-based compounds and provides a new ground states upon compression.

INTRODUCTION

Zintl phases, a unique category of intermetallic compounds, were first introduced by E. Zintl in 1939, and have attracted considerable research attention[1]. Zintl compounds are characterized by their intricate chemical bonding and structural features. Their valence bonding modes can encompass ionic, metallic, and covalent interactions, reflecting their remarkable compositional and structural diversity[2, 3]. Zintl compounds are primarily categorized into layered, chain, cage, etc. These classifications often include AB_2X_2 , $A_5B_2X_6$, AX_3 , and B_4X_3 , with A representing alkali, alkaline-earth or rare-earth metals, B representing transition metals and X representing metalloids[4-12]. With flexible structures, Zintl compounds possess a broad spectrum of physical properties, encompassing superconductivity, topological properties, magnetic order and thermoelectricity, etc[12-19].

In recent years, the layered SnAs-based Zintl compounds have attracted much attention[20-28]. Layered Zintl compound $NaSn_2As_2$ crystallizes in trigonal $R\bar{3}m$ structure, where Na^+ ions are separated by two honeycomb $[SnAs]^{2-}$ layers. The adjacent honeycomb layers interaction is *via* van der Waals (vdW) forces [25, 28]. At ambient pressure, $NaSn_2As_2$ showed bulk superconductivity with T_c of 1.3 K[25, 28]. It should be noted that $NaSn_2As_2$ is a non-electron-balanced compound, containing Sn^{2+} ions with lone pairs of electrons[22, 29]. In contrast to $NaSn_2As_2$, the isostructural compounds $EuSn_2As_2$ is electron-balanced. $EuSn_2As_2$ contains magnetic Eu^{2+} ions, forming a peelable layered magnetic Zintl phase. A transition from paramagnetic (PM) to antiferromagnetic (AFM) phase in $EuSn_2As_2$ occurs around $T_N \sim 24$ K[30-32]. Below T_N , $EuSn_2As_2$ is ferromagnetic in the *ab* plane and antiferromagnetic between adjacent layers, forming an A-type AFM. A combination of first-principles calculations and angle-resolved photoemission spectroscopy (ARPES) experiments reveal that $EuSn_2As_2$ is a magnetic topological insulator (TI), characterizing by the absence of a detectable gap in the Dirac topological surface states (SSs). Besides, $EuSn_2As_2$ transforms from a strong TI with PM state to an axial insulator with AFM state below T_N [33]. T_N shows a linear increase with pressure below 10 GPa, attributed to the enhanced interlayer magnetic exchange coupling among Eu^{2+} ions[34]. Beyond ~ 14 GPa, $EuSn_2As_2$ experiences a two-step high-pressure structural transformation, giving rise to a novel monoclinic configuration. The bent Sn-Sn bonds become planar and form honeycomb Sn sheets, coinciding with the emergence of superconductivity around 4 K [35, 36].

$SrSn_2As_2$ is the sister compound of $EuSn_2As_2$, and $SrSn_2As_2$ remains relatively less explored. Theoretical calculations of the electronic structure propose that $SrSn_2As_2$ is a potential candidate for the novel three-dimensional Dirac semimetal due to its close proximity to the critical point[37]. The ARPES results present a band reversal feature near the Γ point, indicating that $SrSn_2As_2$ may be a new topological insulator[38]. Given that $EuSn_2As_2$ is superconducting accompanied with structure transition under high pressure, it is interesting to explore novel quantum phenomena in $SrSn_2As_2$ upon compression. Hence, we systematically investigate the structural and electronic properties of the SnAs-based Zintl compound $SrSn_2As_2$ under high-pressure. Interestingly, we observed the pressure-induced superconductivity in $SrSn_2As_2$, with a characteristic dome-shaped evolution of T_c . Our theoretical calculations reveal that $SrSn_2As_2$ undergoes a structural transformation from a trigonal to a monoclinic phase under high pressure, as evidenced by both X-ray diffraction (XRD) and Raman data. The electronic band structure of high-pressure phase and the evolution of T_c are also discussed.

EXPERIMENTAL DETAILS and CALCULATION METHODS

The single crystals of SrSn₂As₂ were grown by self-flux method. In order to obtain high-quality single crystals, pretreatment of starting materials (Sn, Alfa Aesar, 99.999% and As, Alfa Aesar, 99.99%) was performed to remove possible oxide layers on their surface by hydrogen reduction method and sublimation recrystallization method. High-purity starting materials of Sr, Sn, and As were loaded into an Al₂O₃ crucible with the atomic ratio of Sr: Sn: As = 1: 2: 2.2, and sealed into a quartz tube in a vacuum of 8×10^{-4} Pa. The raw materials were reacted and homogenized at 1173 K for several hours, followed by cooling down to 773 K at a rate of 3 K/h. The crystalline phase of SrSn₂As₂ was checked by the X-ray diffraction (XRD, Cu $K\alpha$, $\lambda = 1.54184$ Å). The chemical composition of SrSn₂As₂ is given by energy-dispersive x-ray spectra (EDX). Electrical transport properties were performed on a physical property measurement system (PPMS, Quantum Design).

Electrical transport measurements under higher pressures were performed in a nonmagnetic diamond anvil cell (DAC)[39-41]. A cubic BN/epoxy mixture layer was inserted between BeCu gaskets and electrical leads. Four platinum sheet electrodes were touched to the sample for resistance measurements with the van der Pauw method[40, 42, 43]. Pressure was determined by the ruby luminescence method[44]. High-pressure *in situ* Raman spectroscopy investigation was performed using a Raman spectrometer (Renishaw in-Via, UK) with a laser excitation wavelength of 532 nm and a low-wavenumber filter. A symmetric DAC with anvil culet sizes of 300 μm was used, with silicon oil as pressure transmitting medium (PTM). High-pressure *in situ* XRD measurements were performed at beamline BL15U of Shanghai Synchrotron Radiation Facility (X-ray wavelength $\lambda = 0.6199$ Å). A symmetric DAC with anvil culet sizes of 200 μm and Re gaskets were used. Silicon oil was used as the PTM. The two-dimensional diffraction images were analyzed using the FIT2D software[45]. Rietveld refinements of crystal structure under various pressures were performed using the GSAS and the graphical user interface EXPGUI[46, 47].

We used the machine learning graph theory accelerated crystal structure search method (Magus) to explore the structures of SrSn₂As₂ under 30 GPa and 50 GPa[48, 49]. We performed the geometry optimization using the Vienna Ab-initio Simulation Package (VASP) based on the density functional theory [50, 51]. The exchange-correlation functional was treated by the generalized gradient approximation of Perdew, Burke, and Ernzerhof [52]. The calculations used projector-augmented wave (PAW) approach to describe the core electrons and their effects on valence orbitals[53]. The plane-wave kinetic-energy cutoff was set to 600 eV, and the Brillouin zone was sampled by the Monkhorst-Pack scheme of $2\pi \times 0.03$ Å⁻¹. The convergence tolerance was 10^{-6} eV for total energy and 0.003 eV/Å for all forces. The electronic structure calculations used a denser k-mesh grid of $2\pi \times 0.02$ Å⁻¹. The phonon spectrum were calculated by the PHONOPY program package using the finite displacement method with the supercell $2 \times 2 \times 2$ [54].

RESULTS AND DISCUSSION

Prior to high-pressure measurements, we first check the sample quality by single-crystal and powder XRD diffractions. The single-crystal XRD patterns on the flat surface of the sample shows sharp (001) diffraction peaks [Figure 1(a)]. The calculated lattice parameter is $c = 26.66$ Å, in agreement with the previous report[20]. The inset of Fig. 1(b) is the chemical compositional analysis results using EDX, illustrating a Sr:Sn:As atomic ratio of 20.45:38.97:40.59, which is consistent with the nominal composition. In addition, we further performed the powder XRD for structure

characterizing. As shown in Fig. 1(b), all the Bragg peaks can be indexed into rhombohedral symmetry with the space group $R\bar{3}m$. The consistence between powder and single crystal XRD measurements guarantees the correct phase. The ambient crystal structure of SrSn_2As_2 is shown in Figure 1(c), which is identical to the configuration of EuSn_2As_2 and NaSn_2As_2 . Then, we performed transport measurements at ambient pressure. Figure 1(d) shows the resistivity of SrSn_2As_2 as a function of temperature, showing typical metallic behavior with residual resistivity ratio (RRR) = 2.31.

Since NaSn_2As_2 showed superconductivity at ambient pressure and EuSn_2As_2 achieved superconductivity upon compression, it is natural to explore superconductivity in SrSn_2As_2 using high pressure technology. Hence, we investigated the effect of high-pressure on SrSn_2As_2 single crystals. Figure 2(a) shows the electrical resistivity $\rho(T)$ of SrSn_2As_2 at different pressures. Increasing pressure induces a continuous suppression of the overall magnitude of $\rho(T)$, which is typical behavior of metal under high pressure. At 14.9 GPa, the resistivity of SrSn_2As_2 drops abruptly at 1.8 K [Figure 2(b)]. As shown in Fig. 2(b), the resistivity dropped around 3 K and becomes more pronounced upon further compressing. Above 28.3 GPa, zero resistivity is observed at low temperatures, indicating a superconducting transition. The superconducting transition temperature T_c (90% drop of the normal state resistivity) reaches 4.63 K at $P = 28.3$ GPa. As plotted in Fig. 2(c), T_c decreases slowly beyond this pressure, and the superconductivity persists up to 53.5 GPa. The temperature dependence of transition width ΔT_c (10%–90% of the normal state resistance at T_c) is in Fig. 6. The transition width ΔT_c has a sharp decline from 2.07 K to 0.44 K in the pressure range from 22.9 GPa to 34.4 GPa. Transition width ΔT_c reflects the superconducting stated disturbance originating from the thermodynamic fluctuations, the applied magnetic field, the presence of secondary crystalline phases, the applied pressure, etc. [55], which needs further evidence to confirm its origin. The overall behavior of T_c is a typical dome-like evolution under high pressure. Interestingly, a dome-like T_c is observed during decompression, and the superconducting transition persists until recovery to 14.9 GPa (Fig. S1 in the Supplemental Material).

To gain insight into the superconducting transition, we applied an external magnetic field of 28.3 GPa and 48.01 GPa during the rise and fall of T_c on SrSn_2As_2 , respectively. Figure 2(d) and (e) demonstrate that the T_c is continuously suppressed with increasing magnetic field and the superconducting transition could not be observed above 1.8 K at around 2.5 T. This confirms that the sharp drop of $\rho(T)$ around 4 K in SrSn_2As_2 originates from a pressure-induced superconducting transition. The upper critical field $\mu_0 H_{c2}$ is determined from the 90% point on the resistivity transition curve, and the plot of temperature normalized $H_{c2}(T)$ is shown in Fig. 2(f). By fitting the data using the Ginzburg-Landau (GL) formula $\mu_0 H_{c2}(T) = \mu_0 H_{c2}(0) (1 - t^2)/(1 + t^2)$, where $t = T/T_c$ is the reduced temperature with zero-field superconducting T_c . The extrapolated upper critical fields $\mu_0 H_{c2}(0)$ at 28.3 GPa and 48.1 GPa are 2.05 T and 2.41 T, which yields a Ginzburg-Landau coherence length $\xi_{\text{GL}}(0)$ of 12.68 nm and 11.69 nm, respectively.

The transition width ΔT_c drastic changed at around 30 GPa, and the slopes of dH_{c2}/dT are notably different: -0.53 and -0.69 T/K for 28.3 and 48.1 GPa, respectively. Our results suggest that the nature of the superconducting state beyond 30 GPa may differ from that of the initial superconducting one. In order to identify the structural stability of SrSn_2As_2 under high pressure, we have performed high-pressure *in situ* synchrotron XRD and Raman spectroscopy measurements, as shown in Fig. 3. The XRD patterns of SrSn_2As_2 collected at different pressures are shown in Fig.

3(a). As the pressure increases, all diffraction peaks move to higher angles due to lattice contraction, and no structural phase transition is observed at pressures up to 29.8 GPa. Above 33.0 GPa, additional diffraction peaks appear, indicating a structural phase transition. Fig. 3(b) presents the Raman spectra of bulk SrSn₂As₂ under various pressures up to 55.5 GPa. With increasing pressure, the interaction force between adjacent layers increases and all four phonon modes exhibit blue-shift, which is analogous to EuSn₂As₂[36]. The Raman signals of the A_{1g}^2 mode become significant, while E_g^2 mode decreases monotonically. An abrupt disappearance of Raman peaks for pressure beyond 33.6 GPa indicates the structural phase transition to a high-pressure phase. The evolution of the Raman spectra is consistent with our synchrotron XRD patterns and provides further evidence for pressure-induced structural phase transitions.

It should be emphasized that by only relying on the experimental data, the structural solution of high-pressure phases is not possible, because the XRD peaks are rather weak and broad. Hence, we performed the structure predictions at 30 GPa and 50 GPa. In each searching, structures were evaluated within 25 generations with 30 structures per generation, and the ambient stable structure $R\bar{3}m$ was treated as seed structure. We found one stable candidate $C2/m$ phase under high pressure, as shown in the inset of Fig. 4(a). The buckled Sn-Sn bonds become planar and form honeycomblike Sn sheets, meanwhile the SnAs layers further connect to each other *via* the As-As bonds across the Sr layers to form zigzag As chains between the Sn sheets. This three-dimensional monoclinic structure comprising honeycomblike Sn sheets and zigzag As chains resembles the situation in EuSn₂As₂ identified under high pressure [35]. As the enthalpy difference relative to $R\bar{3}m$ structure in Fig. 4(a), the enthalpy of $C2/m$ structure is below that of $R\bar{3}m$ above 22 GPa, suggesting that $C2/m$ structure is more energetically stable under high pressure. Then we calculated the phonon spectrum of $C2/m$ structure under high pressure, as plotted in Fig. 4(b) and (c). There are no imaginary frequencies in the phonon dispersion of $C2/m$ above 25 GPa, illustrating its dynamical stability. In summary, our theoretical and experimental results suggest that there is a structural phase transition from $R\bar{3}m$ phase to $C2/m$ phase under high pressure.

Next, we calculated the electronic structures of $C2/m$ structure under high pressure. As depicted in Fig. 5 (a) and (c), the valence bands and conduction bands cross the Fermi energy in the band structures of $C2/m$ phase, exhibiting typical metal characteristics. We can observe steep conduction bands crossing the Fermi energy, which is beneficial for superconductivity. The corresponding partial density of states (PDOS) are in Fig. 5 (b) and (d). The Sn atoms make main contribution at the Fermi energy, and the total density of states (DOS) at Fermi energy $N(E_f)$ decrease from 5.2 states/formula at 25 GPa to 4.1 states/formula at 50 GPa, which agrees with the slow decreasing of T_c from 28.3 GPa to 53.5 GPa.

Based on the aforementioned results, we can establish a T_c - P phase diagram for SrSn₂As₂ as shown in Fig. 6. Superconductivity was observed at around 20.8 GPa. A domelike evolution is observed with a maximum T_c of 4.63 K at 28.3 GPa for SrSn₂As₂. The high pressure *in-situ* synchrotron XRD and Raman spectroscopy reveal the evidence of structural transition around 28.3 GPa, which is in line with the theoretical predictions that the ambient $R\bar{3}m$ phase transforms to the high-pressure $C2/m$ phase. Combining the transition width results and theoretical calculations, the T_c - P phase diagram reveals two distinct superconducting regions: SC-I $R\bar{3}m$ phase and SC-II $C2/m$ phase. In the SC-I region, T_c increases with pressure with a broaden superconducting transition width. In the SC-II region between 25 and 60 GPa, T_c is monotonically suppressed with external

pressure. The suppression of T_c in SrSn₂As₂ under pressure can be attributed to a decline in electronic density of states at the Fermi level.

CONCLUSION

In summary, we have synthesized SrSn₂As₂ single crystal and explored the structure and electronic transport properties under high pressure. Our results demonstrate a pressure-induced superconductivity in SrSn₂As₂. The pressure dependent T_c follows a dome-like evolution with a maximum T_c value of 4.63 K at 28.3 GPa. Our theoretical calculations, together with high-pressure *in-situ* X-ray diffraction, Raman spectroscopy measurements, indicate that SrSn₂As₂ transforms from the ambient phase $R\bar{3}m$ to the monoclinic $C2/m$ phase above 25 GPa. Our research provides valuable insights into the understanding of the superconductivity in the layered SnAs-based family.

ACKNOWLEDGMENT

This work was supported by the National Natural Science Foundation of China (Grant Nos. 52272265, U1932217, 11974246, 12004252), the National Key R&D Program of China (Grant No. 2018YFA0704300), and Shanghai Science and Technology Plan (Grant No. 21DZ2260400). Z.W.W. thanks the support from the National Key R&D Program of China (Grant Nos. 2020YFA0308800 and 2022YFA1403400), the Natural Science Foundation of China (Grant No. 92065109), the Beijing Natural Science Foundation (Grant Nos. Z210006 and Z190006). The authors thank the Analytical Instrumentation Center (# SPST-AIC10112914), SPST, ShanghaiTech University and the Analysis and Testing Center at Beijing Institute of Technology for assistance in facility support. The authors thank the staffs from BL15U1 at Shanghai Synchrotron Radiation Facility for assistance during data collection.

REFERENCES

- [1] E. Zintl, Intermetallische verbindungen, *Angewandte Chemie*, 52 (1939) 1-6.
- [2] J.D. Corbett, Polyanionic Clusters and Networks of the Early p-Element Metals in the Solid State: Beyond the Zintl Boundary, *Angewandte Chemie International Edition*, 39 (2000) 670-690.
- [3] C. Belin, R.G. Ling, The intermetallic phases of gallium and alkali metals. Interpretation of the structures according to Wade's electron-counting methods, *Journal of Solid State Chemistry*, 48 (1983) 40-48.
- [4] P. Alemany, M. Lluell, E. Canadell, Roles of cations, electronegativity difference, and anionic interlayer interactions in the metallic versus nonmetallic character of Zintl phases related to arsenic, *Journal of computational chemistry*, 29 (2008) 2144-2153.
- [5] C. Zheng, R. Hoffmann, R. Nesper, H.G. Von Schnering, Site preferences and bond length differences in CaAl₂Si₂-type Zintl compounds, *Journal of the American Chemical Society*, 108 (1986) 1876-1884.
- [6] E.S. Toberer, A. Zevalkink, N. Crisosto, G.J. Snyder, The Zintl compound Ca₅Al₂Sb₆ for low-cost thermoelectric power generation, *Advanced Functional Materials*, 20 (2010) 4375-4380.
- [7] P. Rosa, Y. Xu, M. Rahn, J. Souza, S. Kushwaha, L. Veiga, A. Bombardi, S. Thomas, M. Janoschek, E. Bauer, Colossal magnetoresistance in a nonsymmorphic antiferromagnetic insulator, *npj Quantum Mater.*, 5 (2020) 52.
- [8] Y. Tang, Z.M. Gibbs, L.A. Agapito, G. Li, H.-S. Kim, M.B. Nardelli, S. Curtarolo, G.J. Snyder,

Convergence of multi-valley bands as the electronic origin of high thermoelectric performance in CoSb₃ skutterudites, *Nat. Mater.*, 14 (2015) 1223-1228.

[9] C. Pei, T. Ying, Q. Zhang, X. Wu, T. Yu, Y. Zhao, L. Gao, C. Li, W. Cao, Q. Zhang, Caging-pnictogen-induced superconductivity in skutterudites IrX₃ (X= As, P), *Journal of the American Chemical Society*, 144 (2022) 6208-6214.

[10] G.J. Snyder, M. Christensen, E. Nishibori, T. Caillat, B.B. Iversen, Disordered zinc in Zn₄Sb₃ with phonon-glass and electron-crystal thermoelectric properties, *Nat. Mater.*, 3 (2004) 458-463.

[11] J.-S. Rhyee, K.H. Lee, S.M. Lee, E. Cho, S.I. Kim, E. Lee, Y.S. Kwon, J.H. Shim, G. Kotliar, Peierls distortion as a route to high thermoelectric performance in In₄Se_{3-δ} crystals, *Nature*, 459 (2009) 965-968.

[12] Y. Qi, Z. Gao, L. Wang, D. Wang, X. Zhang, Y. Ma, Superconductivity at 34.7 K in the iron arsenide Eu_{0.7}Na_{0.3}Fe₂As₂, *New J. Phys.*, 10 (2008) 123003.

[13] W. Cao, H. Yang, Y. Li, C. Pei, Q. Wang, Y. Zhao, C. Li, M. Zhang, S. Zhu, J. Wu, Pressure-induced Superconductivity in Zintl Topological Insulator SrIn₂As₂, *arXiv preprint arXiv:2307.15629*, DOI (2023).

[14] C. Pei, T. Ying, Y. Zhao, L. Gao, W. Cao, C. Li, H. Hosono, Y. Qi, Pressure-induced reemergence of superconductivity in BaIr₂Ge₇ and Ba₃Ir₄Ge₁₆ with cage structures, *Matter and Radiation at Extremes*, 7 (2022).

[15] J. Wang, T. Ying, J. Deng, C. Pei, T. Yu, X. Chen, Y. Wan, M. Yang, W. Dai, D. Yang, Superconductivity in an Orbital-Reoriented SnAs Square Lattice: A Case Study of Li_{0.6}Sn₂As₂ and NaSnAs, *Angewandte Chemie*, 135 (2023) e202216086.

[16] L.-Y. Feng, R.A.B. Villaos, A.B. Maghirang III, Z.-Q. Huang, C.-H. Hsu, H. Lin, F.-C. Chuang, Prediction of topological Dirac semimetal in Ca-based Zintl layered compounds CaM₂X₂ (M= Zn or Cd; X= N, P, As, Sb, or Bi), *Scientific reports*, 12 (2022) 4582.

[17] A.M. Goforth, P. Klavins, J.C. Fettinger, S.M. Kauzlarich, Magnetic properties and negative colossal magnetoresistance of the rare earth zintl phase EuIn₂As₂, *Inorg. Chem.*, 47 (2008) 11048-11056.

[18] E.S. Toberer, A.F. May, G.J. Snyder, Zintl chemistry for designing high efficiency thermoelectric materials, *Chemistry of Materials*, 22 (2010) 624-634.

[19] C. Chen, W. Xue, S. Li, Z. Zhang, X. Li, X. Wang, Y. Liu, J. Sui, X. Liu, F. Cao, Zintl-phase Eu₂ZnSb₂: A promising thermoelectric material with ultralow thermal conductivity, *Proc. Natl. Acad. Sci. U.S.A.*, 116 (2019) 2831-2836.

[20] K. Shinozaki, Y. Goto, K. Hoshi, R. Kiyama, N. Nakamura, A. Miura, C. Moriyoshi, Y. Kuroiwa, H. Usui, Y. Mizuguchi, Thermoelectric Properties of the As/P-Based Zintl Compounds EuIn₂As_{2-x}P_x (x=0-2) and SrSn₂As₂, *ACS Applied Energy Materials*, 4 (2021) 5155-5164.

[21] K. Lee, D. Kaseman, S. Sen, I. Hung, Z. Gan, B. Gerke, R. Pottgen, M. Feyngenson, J.r. Neuefeind, O.I. Lebedev, Intricate Short-Range Ordering and Strongly Anisotropic Transport Properties of Li_{1-x}Sn_{2+x}As₂, *Journal of the American Chemical Society*, 137 (2015) 3622-3630.

[22] Z. Lin, G. Wang, C. Le, H. Zhao, N. Liu, J. Hu, L. Guo, X. Chen, Thermal conductivities in NaSnAs, NaSnP, and NaSn₂As₂: Effect of double lone-pair electrons, *Phys. Rev. B*, 95 (2017) 165201.

[23] A.M. Ochs, P. Gorai, Y. Wang, M.R. Scudder, K. Koster, C.E. Moore, V. Stevanovic, J.P. Heremans, W. Windl, E.S. Toberer, Computationally guided discovery of axis-dependent conduction polarity in NaSnAs crystals, *Chemistry of Materials*, 33 (2021) 946-951.

[24] Y. Goto, A. Miura, C. Moriyoshi, Y. Kuroiwa, T.D. Matsuda, Y. Aoki, Y. Mizuguchi, Na_{1-x}Sn₂P₂ as a new member of van der Waals-type layered tin pnictide superconductors, *Scientific reports*, 8 (2018) 12852.

- [25] E. Cheng, J. Ni, F. Meng, T. Ying, B. Pan, Y. Huang, D.C. Peets, Q. Zhang, S. Li, Nodeless superconductivity in the SnAs-based van der Waals-type superconductor NaSn_2As_2 , *Europhysics Letters*, 123 (2018) 47004.
- [26] K. Ishihara, T. Takenaka, Y. Miao, O. Tanaka, Y. Mizukami, H. Usui, K. Kuroki, M. Konczykowski, Y. Goto, Y. Mizuguchi, Evidence for s-wave pairing with atomic scale disorder in the van der Waals superconductor NaSn_2As_2 , *Phys. Rev. B*, 98 (2018) 020503.
- [27] Y. Hao, G. Yosuke, J. Rajveer, M. Akira, M. Chikako, K. Yoshihiro, Enhanced superconductivity by Na doping in SnAs-based layered compound $\text{Na}_{1+x}\text{Sn}_{2-x}\text{As}_2$, *Japanese Journal of Applied Physics*, 58 (2019) 83001-83001.
- [28] Y. Goto, A. Yamada, T.D. Matsuda, Y. Aoki, Y. Mizuguchi, SnAs-based layered superconductor NaSn_2As_2 , *J. Phys. Soc. Jpn.*, 86 (2017) 123701.
- [29] M.D. Nielsen, V. Ozolins, J.P. Heremans, Lone pair electrons minimize lattice thermal conductivity, *Energy & Environmental Science*, 6 (2013) 570-578.
- [30] M. Arguilla, N. Cultrara, Z. Baum, S. Jiang, R. Ross, J. Goldberger, EuSn_2As_2 : an exfoliable magnetic layered Zintl–Klemm phase, *Inorganic Chemistry Frontiers*, 4 (2017) 378-386.
- [31] X. Gui, I. Pletikoscic, H. Cao, H.-J. Tien, X. Xu, R. Zhong, G. Wang, T.-R. Chang, S. Jia, T. Valla, A new magnetic topological quantum material candidate by design, *ACS central science*, 5 (2019) 900-910.
- [32] H.-C. Chen, Z.-F. Lou, Y.-X. Zhou, Q. Chen, B.-J. Xu, S.-J. Chen, J.-H. Du, J.-H. Yang, H.-D. Wang, M.-H. Fang, Negative magnetoresistance in antiferromagnetic topological insulator EuSn_2As_2 , *Chin. Phys. Lett.*, 37 (2020) 047201.
- [33] H. Li, S.-Y. Gao, S.-F. Duan, Y.-F. Xu, K.-J. Zhu, S.-J. Tian, J.-C. Gao, W.-H. Fan, Z.-C. Rao, J.-R. Huang, Dirac surface states in intrinsic magnetic topological insulators EuSn_2As_2 and $\text{MnBi}_{2n}\text{Te}_{3n+1}$, *Phys. Rev. X*, 9 (2019) 041039.
- [34] H. Sun, C. Chen, Y. Hou, W. Wang, Y. Gong, M. Huo, L. Li, J. Yu, W. Cai, N. Liu, Magnetism variation of the compressed antiferromagnetic topological insulator EuSn_2As_2 , *Sci. China: Phys., Mech. Astron.*, 64 (2021) 118211.
- [35] L. Zhao, C. Yi, C.-T. Wang, Z. Chi, Y. Yin, X. Ma, J. Dai, P. Yang, B. Yue, J. Cheng, Monoclinic EuSn_2As_2 : A Novel High-Pressure Network Structure, *Phys. Rev. Lett.*, 126 (2021) 155701.
- [36] L. Zhao, X. Ma, C. Tian, C. Yi, Y. Shi, F. Hong, X. Yu, Y. Han, J.-T. Wang, Raman scattering investigation of structural phase transition in compressed EuSn_2As_2 , *Appl. Phys. Lett.*, 121 (2022).
- [37] Q. Gibson, L.M. Schoop, L. Muechler, L. Xie, M. Hirschberger, N.P. Ong, R. Car, R.J. Cava, Three-dimensional Dirac semimetals: Design principles and predictions of new materials, *Phys. Rev. B*, 91 (2015) 205128.
- [38] L.-Y. Rong, J.-Z. Ma, S.-M. Nie, Z.-P. Lin, Z.-L. Li, B.-B. Fu, L.-Y. Kong, X.-Z. Zhang, Y.-B. Huang, H.-M. Weng, Electronic structure of SrSn_2As_2 near the topological critical point, *Scientific Reports*, 7 (2017) 6133.
- [39] W. Cao, N. Zhao, C. Pei, Q. Wang, Q. Zhang, T. Ying, Y. Zhao, L. Gao, C. Li, N. Yu, Pressure-induced superconductivity in the noncentrosymmetric Weyl semimetals LaAlX ($X = \text{Si, Ge}$), *Phys. Rev. B*, 105 (2022) 174502.
- [40] C. Pei, J. Zhang, Q. Wang, Y. Zhao, L. Gao, C. Gong, S. Tian, R. Luo, M. Li, W. Yang, Pressure-induced superconductivity at 32 K in MoB_2 , *National Science Review*, 10 (2023) nwad034.
- [41] Q. Wang, P. Kong, W. Shi, C. Pei, C. Wen, L. Gao, Y. Zhao, Q. Yin, Y. Wu, G. Li, Charge density wave orders and enhanced superconductivity under pressure in the kagome metal CsV_3Sb_5 , *Adv. Mater.*, 33 (2021) 2102813.

- [42] C. Pei, J. Zhang, C. Gong, Q. Wang, L. Gao, Y. Zhao, S. Tian, W. Cao, C. Li, Z.-Y. Lu, Distinct superconducting behaviors of pressurized WB_2 and ReB_2 with different local B layers, *Sci. China: Phys., Mech. Astron.*, 65 (2022) 287412.
- [43] W. Cao, Y. Su, Q. Wang, C. Pei, L. Gao, Y. Zhao, C. Li, N. Yu, J. Wang, Z. Liu, Quantum oscillations in noncentrosymmetric Weyl semimetal $SmAlSi$, *Chin. Phys. Lett.*, 39 (2022) 047501.
- [44] H. Mao, J.-A. Xu, P. Bell, Calibration of the ruby pressure gauge to 800 kbar under quasi-hydrostatic conditions, *J. Geophys. Res. Solid Earth*, 91 (1986) 4673-4676.
- [45] A. Hammersley, S. Svensson, M. Hanfland, A. Fitch, D. Hausermann, Two-dimensional detector software: from real detector to idealised image or two-theta scan, *International Journal of High Pressure Research*, 14 (1996) 235-248.
- [46] A.C. Larson, R.B. Von Dreele, General structure analysis system (GSAS)(Report LAUR 86-748), Los Alamos, New Mexico: Los Alamos National Laboratory, DOI (2004).
- [47] B.H. Toby, EXPGUI, a graphical user interface for GSAS, *J Appl Crystallogr*, 34 (2001) 210-213.
- [48] K. Xia, H. Gao, C. Liu, J. Yuan, J. Sun, H.-T. Wang, D. Xing, A novel superhard tungsten nitride predicted by machine-learning accelerated crystal structure search, *Science bulletin*, 63 (2018) 817-824.
- [49] H. Gao, J. Wang, Y. Han, J. Sun, Enhancing crystal structure prediction by decomposition and evolution schemes based on graph theory, *Fundamental Research*, 1 (2021) 466-471.
- [50] G. Kresse, J. Furthmüller, Efficient iterative schemes for ab initio total-energy calculations using a plane-wave basis set, *Phys. Rev. B*, 54 (1996) 11169.
- [51] H.J. Monkhorst, J.D. Pack, Special points for Brillouin-zone integrations, *Phys. Rev. B*, 13 (1976) 5188.
- [52] J.P. Perdew, K. Burke, M. Ernzerhof, Generalized gradient approximation made simple, *Phys. Rev. Lett.*, 77 (1996) 3865.
- [53] P.E. Blöchl, Projector augmented-wave method, *Phys. Rev. B*, 50 (1994) 17953.
- [54] A. Togo, I. Tanaka, First principles phonon calculations in materials science, *Scripta Materialia*, 108 (2015) 1-5.
- [55] E.F. Talantsev, K. Stolze, Resistive transition of hydrogen-rich superconductors, *Superconductor Science and Technology*, 34 (2021) 064001.

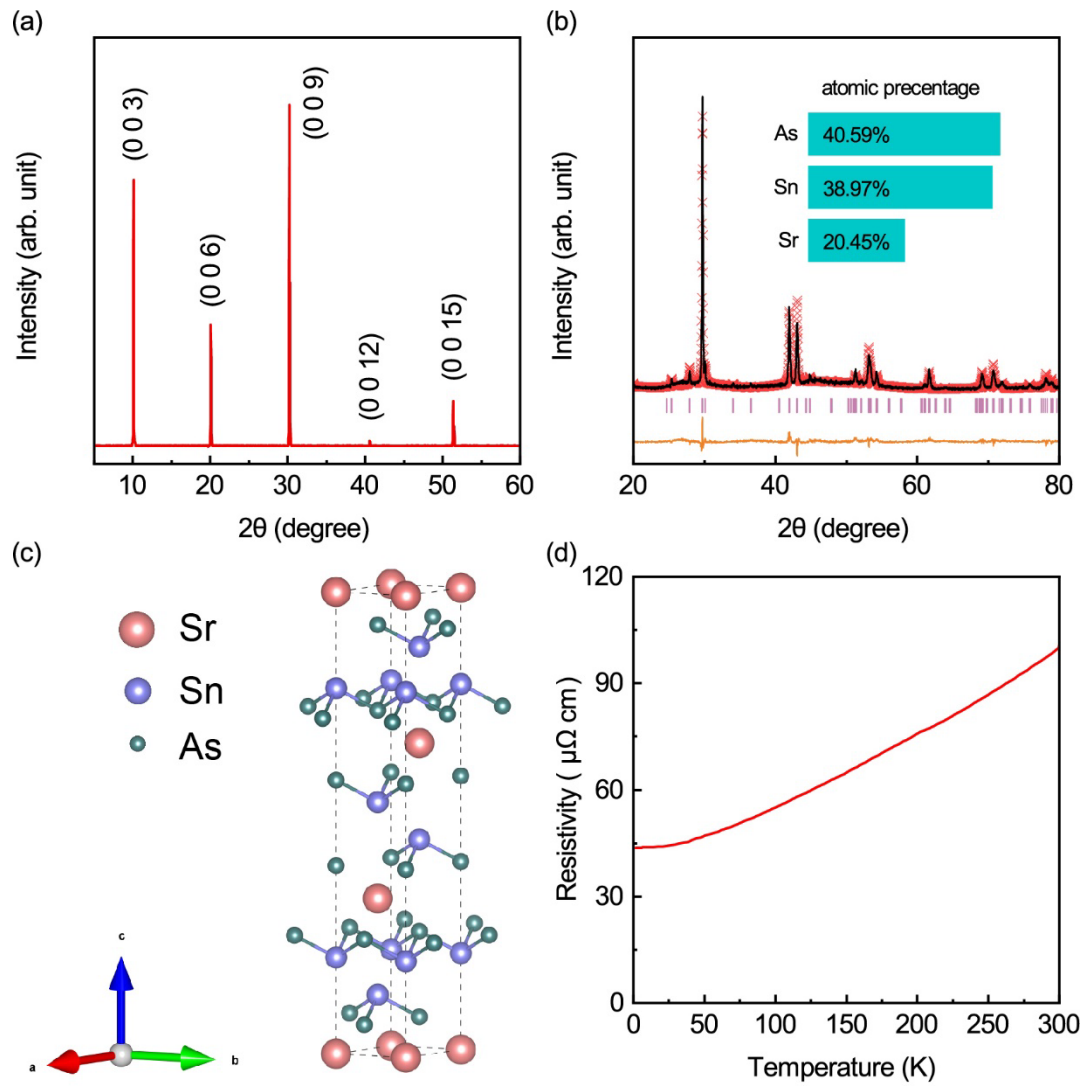


FIG. 1. (a) The crystal structure of SrSn_2As_2 with a space group $R\bar{3}m$. Pink, violet, and green balls represent Sr, Sn, and As atoms, respectively. (b) The X-ray diffraction peaks from the ab plane of SrSn_2As_2 single crystal. (c) Powder XRD pattern of SrSn_2As_2 at room temperature. Inset: the elemental content of SrSn_2As_2 . (d) Resistivity dependence of temperature for SrSn_2As_2 .

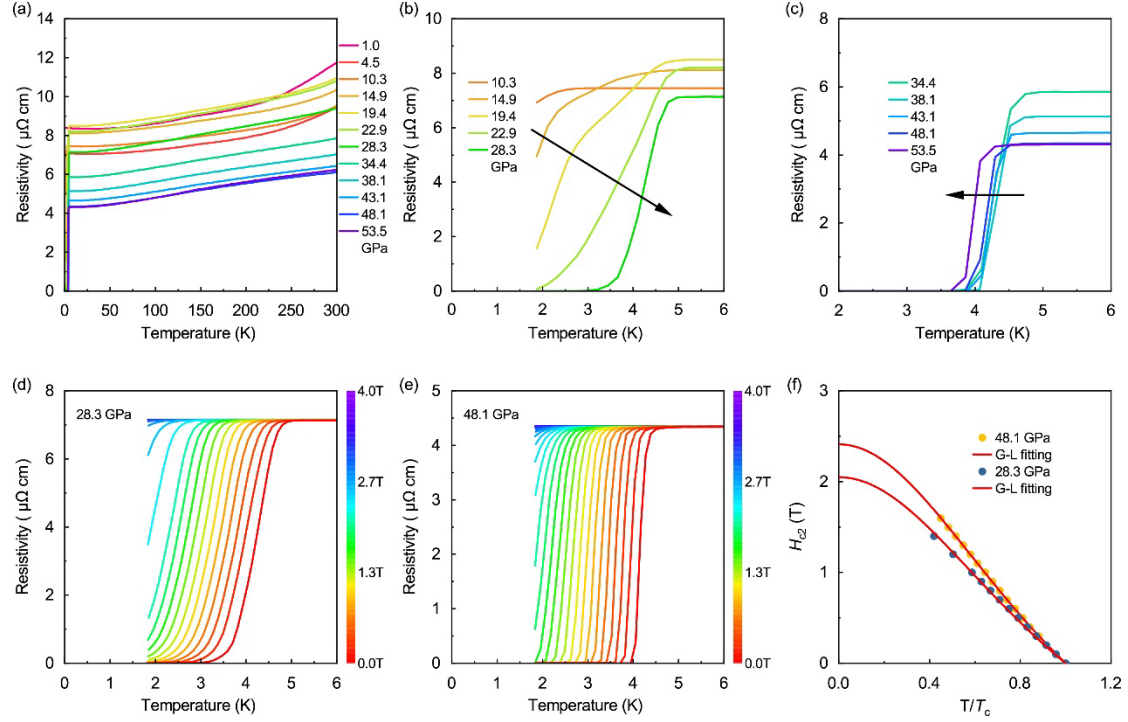


FIG. 2. (a) Pressure dependence of electrical resistivity of SrSn₂As₂ at a temperature range of 1.8–300 K. (b) and (c) Pressure induced superconductivity. The temperature-dependent resistivity under various pressures from 10.3 to 53.5 GPa. (d) and (e) Resistivity of SrSn₂As₂ as a function of temperature under different magnetic fields at pressure of 28.3 GPa and 48.1 GPa, respectively. (f) H_{c2} as a function of normalized temperature at the pressure of SrSn₂As₂ at 28.3 GPa and 48.1 GPa, respectively. T_c is determined as the 90% drop of the normal state resistivity. The solid lines represent the Ginzburg-Landau (G-L) fitting.

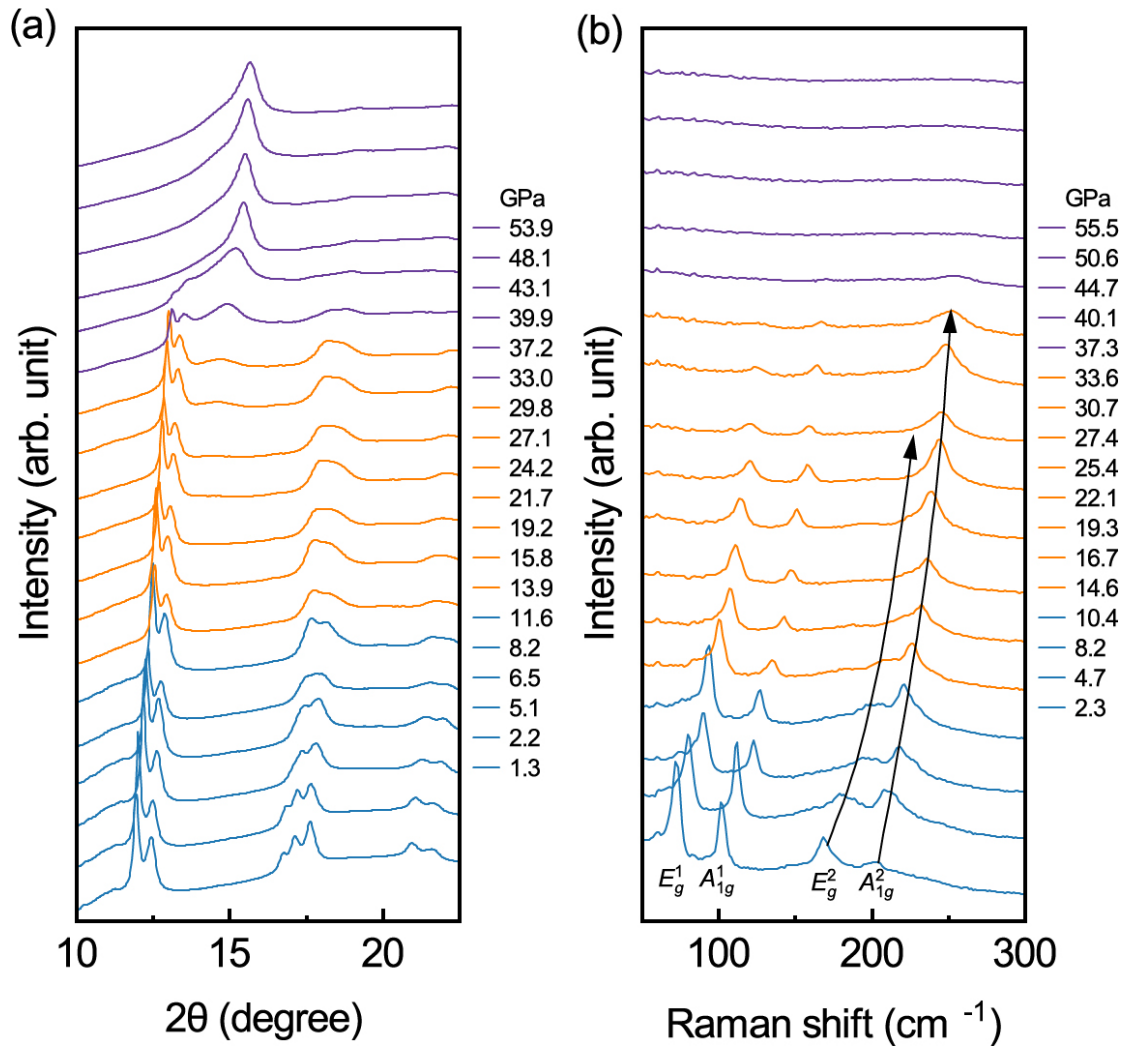


FIG. 3. (a) XRD patterns of SrSn₂As₂ under different pressures up to 53.9 GPa. (b) Raman spectra of SrSn₂As₂ under pressure at room temperature.

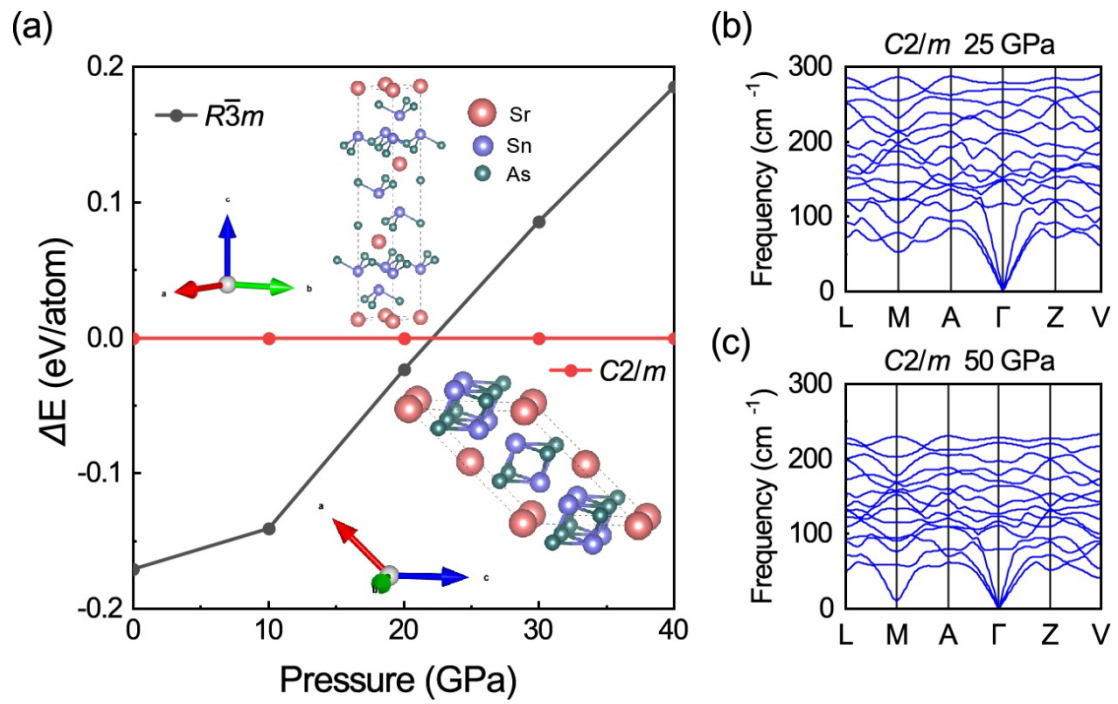


FIG. 4. (a) The enthalpy difference relative to $R\bar{3}m$ structure with in 40 GPa. The calculated phonon spectrum of the predicted $C2/m$ structure at (b) 25 GPa and (c) 50 GPa.

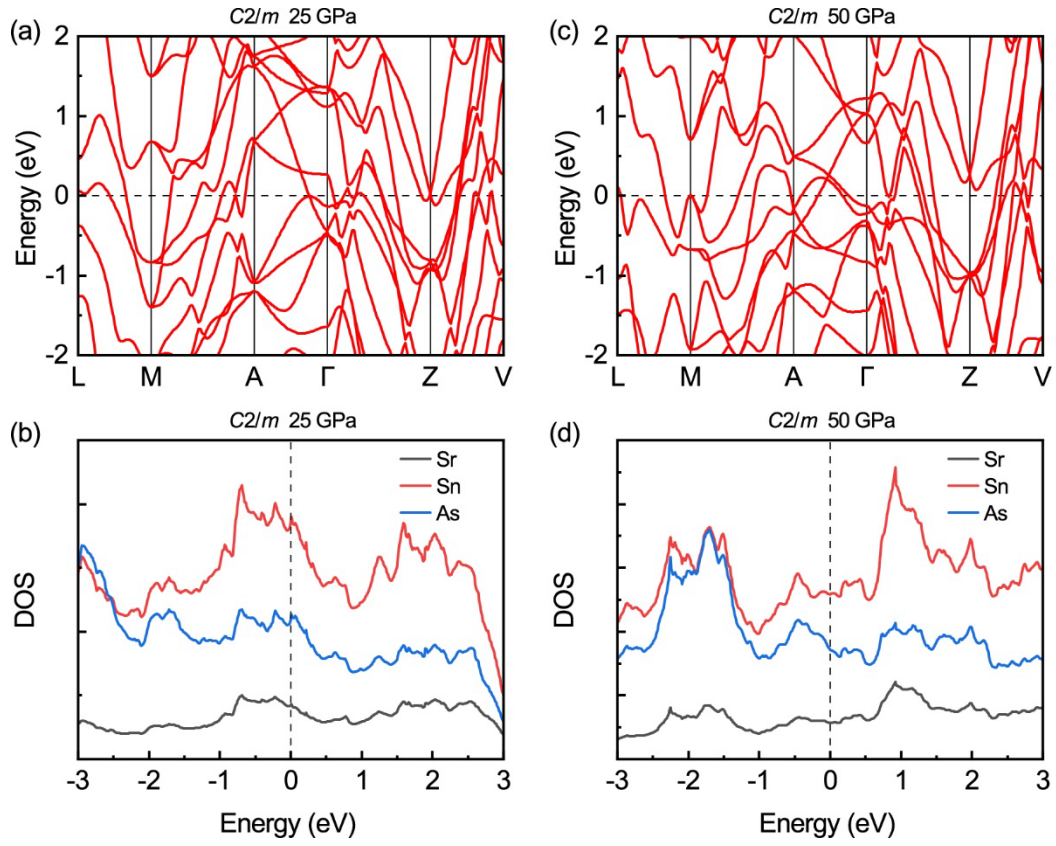


FIG. 5. The band structures of the predicted $C2/m$ structure at (a) 25 GPa and (b) 50 GPa. The corresponding partial density of states (PDOS) at (c) 25 GPa and (d) 50 GPa, respectively. The Fermi energy

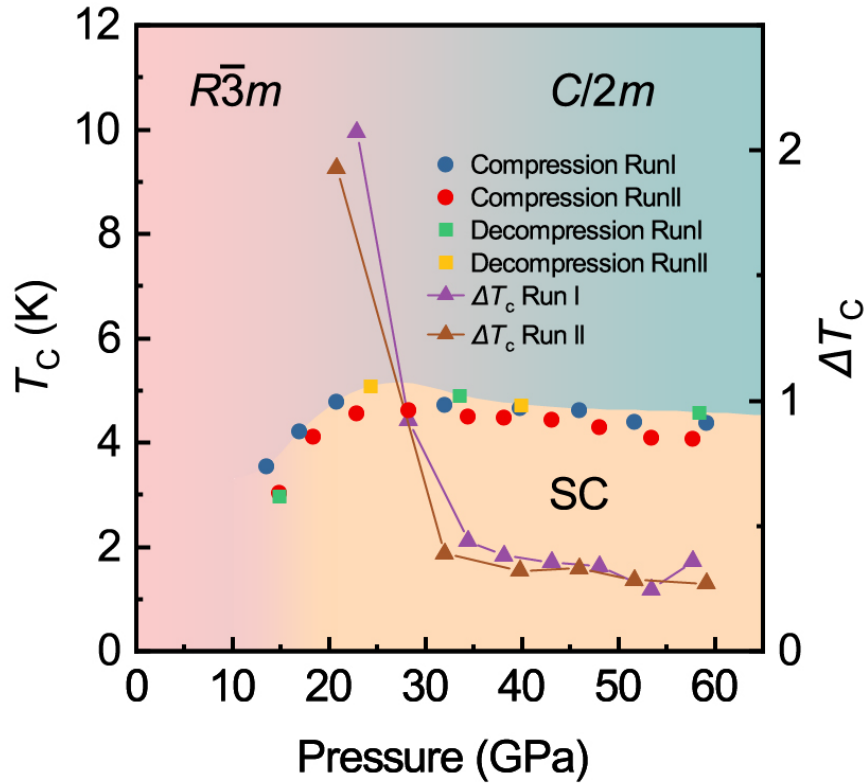


FIG.6. Phase diagram of SrSn₂As₂. Blue, red solid circles and green, yellow solid squares represent the T_c in different compression and decompression experimental runs, respectively. The left vertical axis represents superconducting transition temperature. The beige background represents the superconducting transition temperature. A domelike evolution is observed with a maximum T_c of 4.63 K at 28.3 GPa for SrSn₂As₂. The purple and brown triangular lines represent the pressure dependence of the superconducting transition width ΔT_c . The right vertical axis represents superconducting transition width ΔT_c . The pink and cyan backgrounds represent two different structures. SrSn₂As₂ undergoes a structural transformation from $R\bar{3}m$ to $C/2m$ at high pressure.